Journal of Engineering Mathematics (2005) 51: 57–80 © Springer 2005

Flows of inelastic non-Newtonian fluids through arrays of aligned cylinders. Part 1. Creeping flows

P.D.M. SPELT[1,2,3,*], T. SELERLAND[1,**], C.J. LAWRENCE[3] and P.D. LEE[2]
[1]*Centre for Composite Materials, Department of Aeronautics,* [2]*Department of Materials and* [3]*Department of Chemical Engineering, Imperial College London, United Kingdom*

Received 18 February 2004; accepted in revised form 14 May 2004

Abstract. Numerical simulations are presented for flows of inelastic non-Newtonian fluids through periodic arrays of aligned cylinders, for cases in which fluid inertia can be neglected. The truncated power-law fluid model is used to define the relationship between the viscous stress and the rate-of-strain tensor. The flow is shown to be dominated by shear effects, not extension. Numerical simulation results are presented for the drag coefficient of the cylinders and the velocity variance components, and are compared against asymptotically valid analytical results. Square and hexagonal arrays are considered, both for crossflow in the plane perpendicular to the alignment vector of the cylinders (flows along the axes of the array as well as off-axis flows), and for flow along the cylinders. It is shown that the observed strong dependence of the drag coefficient on the power-law index (through which the stress tensor is related to the rate-of-strain tensor) can be described at all solid area fractions by scaling the drag on a cylinder with appropriate velocity and length scales. The velocity variance components show only a weak dependence on the power-law index. The results for steady-state drag and velocity variances are used in an approximate theory for flows accelerated from rest. The numerical simulation data for unsteady flows agree very well with the approximate theory.

Key words: creeping flow, inelastic non-Newtonian fluids, periodic cylinder arrays

1. Introduction

The flow of Newtonian fluids through periodic arrays of cylinders has been studied extensively, mainly because of its importance in many applications in heat and mass transfer equipment. The main issue is the determination of the drag coefficient for a cylinder in the array. This has been solved for creeping flows through square and hexagonal arrays [1, 2] and random arrays [3] for the entire range of solid area fraction, both for (transverse) flow in the plane normal to the alignment vector of the cylinders and for (longitudinal) flow along the cylinders. More recently, the corresponding flows with small-but-finite and intermediate Reynolds number have been studied [4].

Non-Newtonian fluid flow through arrays of cylinders is a model for flows through porous or fibrous media, such as in the manufacture of fibre-reinforced materials. Prior work has mainly concentrated on a sudden increase in pressure drop over arrays when the flow rate is increased beyond a critical value [5–7], which has been attributed to elastic instabilities that

*Present address: School of Mathematical Sciences, University of Nottingham, Nottingham NG7 2RD, UK.
**Present address: CFD Recipes, Unit 171, Parkers House, 48 Regent Street, Cambridge CB2 1FD, UK.

cause the flow to become three-dimensional [8, 9]. The corresponding critical value of the Deborah number $\mathrm{De} = \lambda U/a$ (where λ is the fluid relaxation time, U is the cell-averaged velocity and a is the cylinder radius) is usually in the range 0·1–1. For values of De below the transition value, the scaled experimental data are virtually independent of De, therefore corresponding to the inelastic limit. The inelastic model used in the present study is therefore appropriate for flows at small but finite Deborah number, $\mathrm{De} \leq 0{\cdot}1$, which are of practical importance for viscoelastic fluids.

A possible complication is that in areas of small rotation and large strain, polymer molecules can be become highly elongated. Stretched molecules resist the extensional flow, leading to very large extensional viscosity values [10]. The converging-diverging nature of flow through arrays of cylinders (and porous media in general) may lead one to expect that the extensional viscosity of polymers should have a significant effect on the flow [6]. However, Talwar and Khomami [11] concluded from two-dimensional steady-state numerical simulations of viscoelastic fluid flows through cylinder arrays that the extensional viscosity has only a modest quantitative effect on the pressure drop over the array, and then only at significant values of De. Liu *et al.* [12] showed that for the flow through a linear periodic array of cylinders confined between two flat plates the effects of elongation are small and that the flow is dominated by the shear flow behaviour of the fluid.

Given the dominance of shear in these flows, and the restriction to low values of De, the fluid rheology may be approximated by a truncated power-law model, *i.e.*, by supposing the stress to be proportional to the shear rate to the power n, where n is the power-law index at large shear rates, and at low shear rates the viscosity to be constant [13, Section 4.6].

In this paper we present a detailed investigation of creeping flows of inelastic fluids through periodic arrays of cylinders using the truncated power-law fluid model. The effects of inertia are the subject of a companion paper [14]. Previous work on these flows is very limited. Tanner [15] studied the flow of a power-law fluid past a single cylinder in an infinite medium. He showed that Stokes' paradox for creeping flows is removed for shear-thinning ($n < 1$) fluids, but not for shear-thickening ($n > 1$) fluids. In cylinder arrays, the shear rate is large near the cylinder surface and zero on axes of symmetry, such that the viscosity varies significantly throughout the flow, which may have a strong effect on the flow structure. It is surprising therefore that in some earlier work the effects of shear-thinning could be scaled out. Since the viscosity is a function of shear rate, a capillary flow model was used in [6] and [7] for power-law fluids to calculate an approximate viscosity value that could be used to collapse their data. Bruschke and Advani [16] presented their results for flows of power-law fluids through cylinder arrays (restricted to flow along an axis of the arrays) in terms of a mobility factor that made the results independent of the power-law index. On the other hand, Tanner [15] and D'Alessio and Pascal [17] found no simple power-law dependence of the drag coefficient for a single cylinder in an infinite medium. (Other related work includes [18], where a cell model is used, rather than a periodic array, as a representation of random aligned fibres. Power-law models have also been used in network models, to determine effective Darcy laws for inelastic fluid flow through porous media [19, 20].) In this paper we aim to clarify the dependence of the drag coefficient on the power-law index for arrays of cylinders with a variety of geometries and flow directions.

The present study is not restricted to the calculation of the drag coefficient of a cylinder in an array, or, equivalently, of the averaged velocity in the bed given the pressure drop over the bed. The drag coefficient is all that is required for the description of steady flow through a homogeneous bed, since an effective Darcy's law is then valid, but for the description of more

general flows, additional quantities are required. The equations of motion that describe general flow through fixed beds can be obtained by ensemble-averaging the fluid flow equations. This does not imply that the fibrous bed is assumed to be random: there may be significant structure as long as the bed as a whole is positioned somewhat differently in each realisation of the flow. The general form of the averaged (bulk) equations of motion is [21], with overbars indicating ensemble-averaged values,

$$\frac{\partial \overline{V}_j}{\partial x_j} = 0, \qquad \rho \frac{\partial \overline{V}_i}{\partial t} + \rho \frac{\partial}{\partial x_j}\left(\overline{V}_i \overline{V}_j\right) = -\rho \frac{\partial}{\partial x_j}\left(\overline{v_i v_j}\right) + \overline{f}_i + \frac{\partial \overline{\sigma}_{ij}}{\partial x_j}, \tag{1}$$

where $\overline{\boldsymbol{V}}$ is the averaged velocity vector (the velocity $\boldsymbol{V}$ is zero inside the cylinders), $\overline{\boldsymbol{\sigma}}$ is the effective stress tensor in the bed, $v_i \equiv V_i - \overline{V}_i$ is the local deviation from the mean velocity and f_i is the force density due to the force exerted by the cylinders on the fluid. We present results for the steady-state drag force in this study, but also address the added mass force contribution that arises in unsteady flows. Darcy's law is obtained from this momentum equation by dropping all spatial and temporal derivatives, apart from the pressure gradient.

The term in (1) that involves the velocity variance $\overline{v_i v_j}$ can become significant compared to the viscous stresses when the Reynolds number based on the bed dimensions is not small, which may be the case while the Reynolds number based on the fibre diameter is still small. Knowing the velocity variances is also useful for other purposes. The drag coefficient can be expressed in terms of the cell-averaged fluid velocity (see (14) below) and any simple scaling for the drag coefficient must therefore be corroborated by even simpler results for the velocity variances. Also, Hill, Koch and Ladd [22] showed recently that for Newtonian fluids the added mass coefficient of a sphere in an array can be related with good approximation to the steady-state velocity variances (the corresponding problem for cylinders is addressed in Section 8).

For these reasons, the numerical simulations of flow through periodic arrays of cylinders presented here have been used to evaluate the velocity variances as well as the drag coefficient. The simulations presented here can not be used for the determination of the effective stress tensor for fixed beds, which would require simulation of shear flow through the array. This problem does not occur for suspensions in which particulates are allowed to move freely, an effective viscosity has been obtained for that case [23, 24]. The effective viscosity for flow of Newtonian fluids through fixed beds can be obtained instead, for instance, by optimising the predictions of the averaged equations for certain test cases, with the effective viscosity as the fitting parameter [25, 26], by using the averaged equations in a self-consistent approximation to obtain the permeability [3], or by using a homogenization technique [27].

We present the equations of motion for truncated power-law fluids in Section 2 below. In Section 3 we describe the numerical method, and in Sections 4 and 5 we present the results for the drag coefficient and velocity variance components, respectively. The results are compared with a lubrication theory for concentrated arrays. The effects of the low-shear Newtonian range and extensional viscosity are addressed in Sections 6 and 7. Results for unsteady flows are presented in Section 8.

2. Equations of motion

Taking $\boldsymbol{V}$ as the velocity vector, P the pressure, $\boldsymbol{\tau}$ the viscous part of the stress tensor, and ρ the density, the full equations of motion are,

$$\frac{\partial V_j}{\partial x_j} = 0, \qquad \rho\frac{\partial V_i}{\partial t} + \rho\frac{\partial}{\partial x_j}\left(V_i V_j\right) = -\frac{\partial P}{\partial x_i} + \frac{\partial \tau_{ij}}{\partial x_j}. \tag{2}$$

For generalised Newtonian viscous fluids, the stress tensor depends on the rate-of-strain tensor through

$$\tau_{ij} = 2\eta E_{ij}, \tag{3}$$

where

$$E_{ij} = \frac{1}{2}\left(\frac{\partial V_i}{\partial x_j} + \frac{\partial V_j}{\partial x_i}\right) \tag{4}$$

is the rate-of-strain tensor and η is a scalar function of the second invariant of the rate-of-strain tensor $\Pi = 2E_{kl}E_{kl}$ (summation over the indices k and l is presumed). For many fluids, the function $\eta(\Pi)$ takes a power-law form ($\eta = K\Pi^{(n-1)/2}$) for sufficiently large values of Π, with a Newtonian plateau ($\eta = \eta_0$ =constant) at small values of Π. Such fluids have a characteristic shear rate $\dot{\gamma}_0 = (\eta_0/K)^{1/(n-1)}$ that marks the transition between the two types of behaviour. Several models have been proposed to describe viscosity functions of this form [13, Chapter 4]. Here we chose the simplest, which is the truncated power-law fluid model:

$$\eta = \begin{cases} K\Pi^{(n-1)/2} & \text{if} \quad \Pi \geq \dot{\gamma}_0^2, \\ \eta_0 & \text{if} \quad \Pi \leq \dot{\gamma}_0^2, \end{cases} \tag{5}$$

where $\dot{\gamma}_0 = (\eta_0/K)^{1/(n-1)}$ and $\Pi = 2E_{kl}E_{kl}$ is the second invariant of the rate-of-strain tensor (summation over the indices k and l is presumed). The power-law fluid model corresponds to the limiting case $\dot{\gamma}_0 \to 0$. K and n are the power-law coefficient and index, respectively; $n < 1$ corresponds to a shear-thinning fluid (*i.e.*, the 'viscosity' (ratio of stress and strain rate) is small in regions of large strain rates), $n = 1$ to a Newtonian fluid and $n > 1$ to a shear-thickening fluid. A general discussion of the effect of fluid microstructure on rheological properties can be found in [28, Chapter 14]. Shear-thinning fluids are much more common than shear-thickening fluids, with usually $n \geq 0{\cdot}2$. This study confines itself to $n \geq 0{\cdot}5$.

The dimensionless number $\Gamma = \dot{\gamma}_0 a/U$, where U is the magnitude of the averaged velocity (that is, the velocity averaged over the unit cell) and a is the cylinder radius, is a measure of the relative importance of the low-shear-rate Newtonian plateau. Initially we have used small values for Γ in order to expose as much as possible of the fluid to the non-Newtonian rheology: the value of Γ is small enough not to affect the results, unless indicated otherwise. In Section 6 we investigate the effect of increasing Γ.

Making the momentum equation dimensionless yields the Reynolds number $\mathrm{Re} \equiv \rho a^n U^{2-n}/K$, where we have used the cylinder radius as the charateristic length scale of the flow to scale the viscosity. Flows at finite Reynolds numbers are the subject of a companion paper [14] and we shall restrict ourselves here to low-Reynolds-number flows. The Reynolds number becomes independent of the velocity at $n = 2$, but we shall consider values of n not larger than 1·5. The range of values of n that we consider in this study is therefore $0{\cdot}5 \leq n \leq 1{\cdot}5$.

The velocity field for creeping on-axis flow of a Newtonian fluid through a periodic array has fore/aft symmetry (the velocity is an even, and the pressure an odd, function of position), resulting from the linearity of the equations of motion and the symmetry of the geometry. Although the equations of motion for creeping flows of power-law fluids are not linear, and a superposition principle does not hold, the resulting velocity field exhibits the same fore/aft symmetry in that case as well. This is the result of the underlying linearity in (2), and Π in (5) not changing sign when the sign of the velocity vector is changed. We have however not made use of this symmetry in our calculations.

3. Numerical method

We have adopted here an extension of the numerical method proposed by Zang, Street and Koseff [29] for Newtonian fluids. Although this method has been documented extensively in their paper (see also [30]) and has been used for a variety of problems, including large-eddy simulations of jets [31], the motion of rising bubbles [32, Chapter 6] and other free-surface flows [33], it is necessary to present this method in some detail here to explain how we have accounted for the rheology of truncated power-law fluids. In regions of the flow where the shear rate is small enough for the fluid to be Newtonian the method becomes identical to that of Zang, Street and Koseff [29].

The method of Zang, Street and Koseff [29] is a finite-difference, fractional step method using a non-staggered, body-fitted grid. The equations of motion are transformed from co-ordinates x_i into generalised coordinates ξ_i and written in strong-conservation law form:

$$\frac{\partial}{\partial \xi_m}\left(\beta_k^m V_k\right) = 0, \qquad \frac{\partial\left(J^{-1}\rho V_i\right)}{\partial t} + \frac{\partial F_{im}}{\partial \xi_m} = 0 \tag{6}$$

with

$$F_{im} \equiv \rho\beta_k^m V_i V_k + \beta_i^m P - K\,\Pi^{(n-1)/2}\left(G^{mk}\frac{\partial V_i}{\partial \xi_k} + \beta_j^m b_i^k \frac{\partial V_j}{\partial \xi_k}\right). \tag{7}$$

Here $J \equiv 1/\det\left(\partial x_i/\partial \xi_j\right)$ is the Jacobian of the transformation, $\beta_i^m \equiv J^{-1}\left(\partial \xi_m/\partial x_i\right)$, $b_i^m \equiv \partial \xi_m/\partial x_i$, $G^{jm} \equiv \beta_k^j b_k^m$ is the mesh skewness tensor, and

$$\Pi = \frac{1}{2}\left(b_j^m \frac{\partial V_i}{\partial \xi_m} + b_i^q \frac{\partial V_j}{\partial \xi_q}\right)\left(b_j^r \frac{\partial V_i}{\partial \xi_r} + b_i^s \frac{\partial V_j}{\partial \xi_s}\right). \tag{8}$$

The generalised coordinates are defined so that the computational domain becomes a square mesh, where the velocity components and pressure are calculated at the centre of each computational cell. Having written the momentum equation in strong conservation law form (6), the spatial derivatives become the net addition of momentum fluxes into each cell. The momentum flux through each cell face is approximated using the neighbour cell-centred velocity components and pressure of neighbouring cells. The geometrical terms are approximated using the coordinates of cell vertices for β_i^m, while b_i^m is calculated from the coordinates of cell centres.

Our extension of Zang, Street and Koseff's [29] method is to allow the 'viscosity' to depend on the rate of strain. As the viscosity only enters the equations of motion through the flux (7), we have evaluated it similarly to the other terms on the right-hand side of (7), *i.e.*, at cell faces using cell-centred velocities of the neighbouring cells.

To show how this changes the time-stepping procedure we shall now briefly summarise Zang, Street and Koseff's [29] method in more detail. At each timestep, denoted by a superscript q, first a predictor step is made (resulting in a velocity field $\mathbf{V}^*$) without the pressure term in (7). The Crank-Nicolson method is used for the viscous terms and the Adams-Bashforth method for the convective terms. All off-diagonal viscous terms are treated explicitly; even in the diagonal viscous terms that are treated implicitly, the velocity gradients used in the calculation of Π in (8) are kept explicit. The predictor step is, for a timestep Δt,

$$\left(I - \frac{J\Delta t}{2} D_I\right)\left(V_i^* - V_i^q\right) = J\Delta t \left[\frac{3}{2}\left(C_i^q + D_{E1}\left(V_i^q\right) + D_{E2}\left(V_j^q\right)\right) - \frac{1}{2}\left(C_i^{q-1} + D_E\left(V_i^{q-1}\right) + D_{E2}\left(V_j^{q-1}\right)\right) + D_I\left(V_i^q\right)\right], \tag{9}$$

where we have used the notation

$$C_i^q \equiv -\frac{\delta}{\delta\xi_m}\left(\beta_j^m V_i^q V_j^q\right), \qquad D_I \equiv K\frac{\delta}{\delta\xi_m}\left(\Pi^{(n-1)/2} G^{mk}\frac{\delta}{\delta\xi_k}\right) \quad (\mathrm{m} = \mathrm{k}), \tag{10}$$

$$D_{E1} \equiv K\frac{\delta}{\delta\xi_m}\left(\Pi^{(n-1)/2} G^{mk}\frac{\delta}{\delta\xi_k}\right) - D_I, \qquad D_{E2} \equiv K\frac{\delta}{\delta\xi_m}\left(\Pi^{(n-1)/2}\beta_j^m b_i^k\frac{\delta}{\delta\xi_k}\right), \tag{11}$$

and in the calculation (8) of Π for D_I the old velocity field is used. The correction step is to substract the pressure gradient times the timestep from $\mathbf{V}^*$,

$$V_i^{n+1} = V_i^* - J\Delta t\ \rho^{-1}\frac{\delta}{\delta\xi_m}\left(\beta_i^m P^{n+1}\right). \tag{12}$$

Before the correction step is made, the pressure is calculated from the requirement that the corrected velocity field should be incompressible,

$$\frac{\delta}{\delta\xi_m}\left(G^{mk}\frac{\delta P^{q+1}}{\delta\xi_k}\right) = \frac{\rho}{\Delta t}\frac{\delta}{\delta\xi_m}\left(\beta_k^m V_k^*\right). \tag{13}$$

The connection between pressure and velocity is assured by interpolating the values of the velocity components to the cell faces when evaluating the right-hand side of this Poisson equation for the pressure. Zang, Street and Koseff [29] adopted a multigrid method to solve the Poisson equation for the pressure. For our two-dimensional calculations the line Gauss-Seidel method with alternating sweep directions was found to be sufficient.

The usual convergence test case for Newtonian fluid flows, an analytical solution of the Navier-Stokes equations for decaying vortices, yielded results virtually identical to those obtained by Zang, Street and Koseff [29]. No analytical solution for power-law type fluids is available but a convergence test could be carried out for the flow across a square array of cylinders using the symmetry of the problem. The main results of each simulation are the cell-averaged fluid velocity components, $\overline{V}_i$ (*cf.* (14) below). Convergence of this quantity was tested for the case in which the pressure drop over the unit cell was specified to be the same in each direction, such that $\overline{V}_2$ should be equal to $\overline{V}_1$. But the mesh that was used is not symmetric about the diagonal, and a small error results. Convergence tests showed the error $\overline{V}_2/\overline{V}_1 - 1$ to be approximately of second order in the grid spacing. The code was

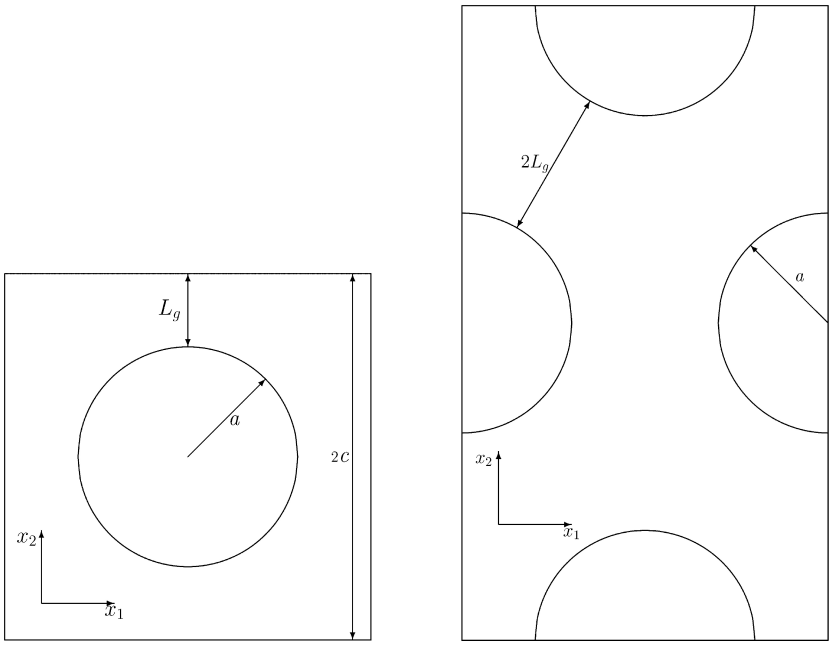

Figure 1. Geometries considered. Unit cell of a square array (a), and a hexagonal array (b). Flow is either in the (x_1,x_2) plane (transverse flow), or along the cylinders (longitudinal flow).

further tested against previous results for several Newtonian flows, for unsteady intermediate Reynolds number simulations of flow through arrays of cylinders [4] and for Stokes flow through arrays of cylinders [1, 3]. In Sections 4 and 5, the results for non-Newtonian fluids are compared with asymptotic theories.

To avoid numerical difficulties, we have restricted our attention to $n \geq 0{\cdot}5$. For lower values of n, significant errors in the pressure were found, particularly in cases where Γ is small.

Equations (6–7) have been solved numerically for flow through a unit cell of a periodic array for both square and hexagonal arrangements of cylinders, as shown in Figure 1. In most cases a mesh of 60×60 was used. In each case a pressure drop was applied over the unit cell and the equations of motion were integrated over time until the solution reached a steady state. The velocity vector is periodic in both directions, while the pressure drop over the unit cell is specified in both directions, *i.e.*, the pressure at the right face is equal to the pressure at the left face minus the horizontal pressure drop, and the pressure at the top face is equal to the pressure at the bottom face minus the vertical pressure drop, which is non-zero for off-axis flows.

4. The drag coefficient

4.1. On-axis transverse flows and longitudinal flows

The pressure drop applied to the unit cell is balanced by the drag force on the cylinders. Therefore, a force balance over the unit cell was used to obtain the drag coefficient. For on-axis flows a simple scaling is used to introduce the drag coefficient C_d,

$$F \equiv C_d(\phi, n)\, \eta\, U, \tag{14}$$

where F is the applied force per unit length of cylinder, η is a fluid viscosity scale, and $U \equiv |\overline{\mathbf{V}}|$. For now we shall use $\eta = \eta_a \equiv K(U/a)^{n-1}$, where a is the cylinder radius. Because F is simply the product of the applied pressure drop over the cell and the length of the side of the cell, and is therefore known, the drag coefficient is obtained from (14) by calculating the cell-averaged fluid velocity U.

4.1.1. *Lubrication theory for concentrated arrays*

For transverse flows at high solid area fractions the pressure drop over the unit cell is almost entirely due to the large pressure drop over the narrow gap between the cylinders. The velocity component in the main flow direction is $O(U/\varepsilon)$, where $\varepsilon = L_g/a$ (see Figure 1). Spatial derivatives in the main flow direction scale with $\varepsilon^{1/2}a$, whereas those perpendicular to the main flow scale with εa. From continuity, it follows that the transverse velocity component is $O(U/\varepsilon^{1/2})$. In the momentum equation, the pressure gradient, which is $O(\Delta p/(a\varepsilon^{1/2}))$, is balanced by the divergence of the viscous stress, which is $O\left(KU^n a^{-n-1}\varepsilon^{-2n-1}\right)$. Hence the pressure drop over each gap is $O(KU^n a^{-n}/\varepsilon^{2n+1/2})$. The full result is, for square arrays with solid area fraction ϕ,

$$C_d = 2^{3/2}\pi^{1/2}\left(\frac{1+2n}{n}\right)^n \frac{\Gamma(2n+\frac{1}{2})}{\Gamma(2n+1)}\left(1-\left(\frac{\phi}{\phi_{\max}}\right)^{1/2}\right)^{-2n-1/2} \qquad (|\phi-\phi_{\max}| \ll 1), \tag{15}$$

with $\phi_{\max} = \pi/4$, the maximum possible solid area fraction [34]. The result for hexagonal arrays is essentially the same as (15), but with an additional factor of $3^{(n+1)/2}/2^n$ on the right-hand side and with $\phi_{\max} = \pi/(2\sqrt{3})$. A lubrication theory has been derived previously by Bruschke and Advani [16]. In their analysis some (but not consistently all) of the higher-order terms are maintained, resulting in a more complex expression that agrees with the result above in the limit of concentrated arrays. A similar lubrication theory for longitudinal flows is not feasible since the flow is dominated by the interstitial regions rather than the narrow gaps.

4.1.2. *Numerical results for on-axis flows*

Figure 2a shows the drag coefficient for on-axis flows through square arrays as a function of the power-law index, at different solid area fractions. A very pronounced dependence on both the solid area fraction and the power-law index is observed. The solid lines show the lubrication result (15), with which the numerical results are seen to agree well for all values of n at high area fractions.

The variation of the drag coefficient with n depends on the choice of viscosity scale in the drag coefficient, (14). We have used here simply the averaged fluid velocity and the cylinder radius in the viscosity scale, *i.e.*, $\eta = \eta_a \equiv K(U/a)^{n-1}$. The shear rate (in Π, see (5)) in the gap between the cylinders scales with the ratio of a velocity scale $U_L \equiv Uc/L$ (with c half

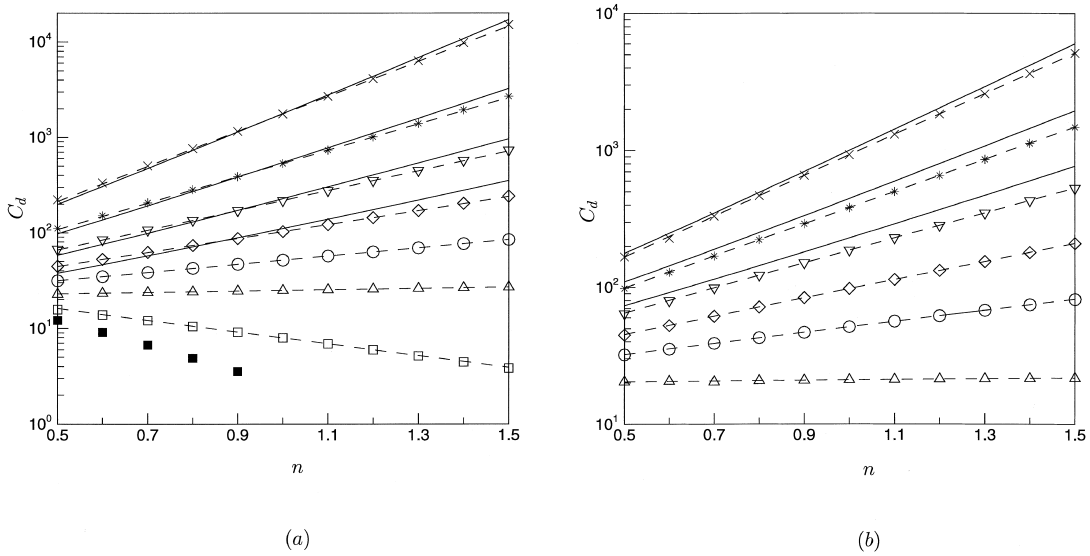

Figure 2. Numerical simulation results for the drag coefficient C_d of a cylinder in a square (*a*) and hexagonal (*b*) array as a function of power-law index n for area fractions 0·01 (□), 0·1 (△), 0·2 (◯), 0·3 (◇), 0·4 (▽), 0·5 (∗) and 0·6 (×). The filled symbols are numerical simulation results by Tanner [15] for a single cylinder in an infinite medium. The solid lines represent the lubrication theory (15). The dashed lines show the scaling result (16).

the height of the unit cell, see Figure 1) and a length scale L. The latter are approximately the averaged velocity in the gaps between the cylinders and half the minimum gap size, respectively. Hence, scaling the shear rate with the velocity averaged over the unit cell and the cylinder radius introduces a dependence of C_d on n.

A new drag coefficient $\tilde{C}_d$ can be introduced by using $\eta = \eta_L \equiv K(U_L/L)^{n-1}$ in (14). In general, $\tilde{C}_d$ will depend on n as well as on ϕ. But we can absorb this dependence into L, so that this new drag coefficient does not depend on n. Then equating both scaling relations of the drag force, the drag coefficient defined by (14) is found to have the following dependence on n:

$$C_d(\phi, n) \equiv C_d(\phi, 1) \left(\frac{\phi}{\phi_{\max}}\right)^{(1-n)/2} \left(\frac{L}{a}\right)^{2-2n} . \tag{16}$$

The value of L/a is thus equal to the ratio $(\phi_{\max}/\phi)^{(1/4)} \times (C_d(\phi, n)/C_d(\phi, 1))^{1/(2-2n)}$. The numerical simulation results for L/a are plotted in Figure 3. If the above argument explains the dependence on n of the drag coefficient seen in Figure 2a, then L/a should be a function of ϕ only. We see that this is indeed the case to a very good approximation for the values of n simulated. There is a small decrease in L/a with decreasing n at low ϕ which is addressed below. The results for L/a inferred from the lubrication theory (15) are also shown, revealing only a small increase in L/a if n is decreased. The scaling is also appropriate at lower values of n than considered here. As $n \downarrow 0$, L/a reaches a constant in the lubrication approximation, $\sqrt{8/9}(\phi_{\max}/\phi)^{1/4}(1-(\phi/\phi_{\max})^{1/2})$, which is only 14% above the value at $n = 1{\cdot}5$ at $\phi = 0{\cdot}6$. After averaging L/a for each ϕ over the whole range of n, equation (16) has been used to plot the values for C_d in Figure 2a (the dashed lines).

Very good agreement was also found for the other geometries considered here, as can be seen in Figure 2b for hexagonal arrays. Denoting the values of L averaged over n by $\mathcal{L}$, the

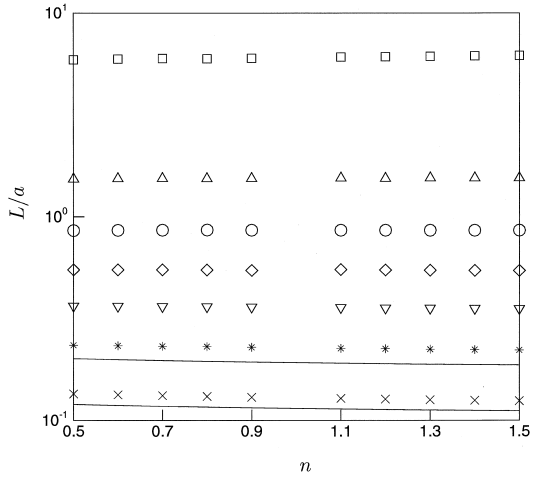

Figure 3. Numerical simulation results for the ratio L/a defined by (16) for a cylinder in a square array, as a function of power-law index n at area fractions 0·01 (□), 0·1 (Δ), 0·2 (◯), 0·3 (◇), 0·4 (∇), 0·5 (∗) and 0·6 (×). The lines are the lubrication theory (15).

resulting normalised values of $\mathcal{L}$ for square and hexagonal geometries are shown in Figure 4, both for on-axis transverse flow and longitudinal flow. Because $\mathcal{L}/a$ changes strongly with area fraction, we have normalised $\mathcal{L}$ with half the minimum gap between the cylinders, $L_g = \left((\phi_{\max}/\phi)^{1/2} - 1\right) a$ (as indicated in Figure 1); the results for transverse flows are close to this gap dimension. The results are larger for longitudinal flows because the fluid is not squeezed through the narrowest gap between the cylinders.

We note here that $\mathcal{L}$ can be interpreted as the appropriate lengthscale of the fluid velocity, and the value of $\mathcal{L}$ is close to L_g, which is a well-defined quantity (Figure 1). More precisely, $\mathcal{L}$ is defined as the length scale that, when used in the choice of viscosity scale η in (14), leads to a drag coefficient with minimal dependence on n. Trying to understand what L is for a Newtonian fluid is not possible since, as is evident from (16), L is not defined for $n = 1$: the viscosity scale in (14) is uniquely defined as the (Newtonian) fluid viscosity. Nevertheless, and perhaps surprisingly, L/a appears to be continuous through $n = 1$ (Figure 3).

The creeping flow equations have no solution for a single cylinder in an infinite Newtonian fluid, because inertial effects cannot be ignored far away from the cylinder. However, Tanner [15] argued, using approximate analysis, that the Stokes paradox does not appear for $n < 1$. He also presented numerical simulation results for the drag coefficient of a single cylinder in a shear-thinning fluid which were obtained with a boundary element method; these are shown in Figure 2a. Tanner's results show a dependence on the power-law index which is similar to that of the present results for periodic arrays. The n-dependence of his results for the drag coefficient can therefore be understood as simply resulting from the length scale that has been used in the drag coefficient definition; the appropriate length scale is nearly 20 times the cylinder radius. The results for the periodic array are seen from Figure 2a to approach Tanner's results for small area fractions.

Bruschke and Advani [16] performed numerical simulations of on-axis creeping flows of power-law fluids through square arrays of cylinders. They presented their results in terms of a dimensionless mobility factor M', which can be shown to be equal to $(\phi_{\max}/\phi)^{1+n}/C_d$. They showed that the quantity $\left(M'(\phi, n)/M'(\phi, 1)\right)^{1/(1-n)}$ is virtually independent of the power-

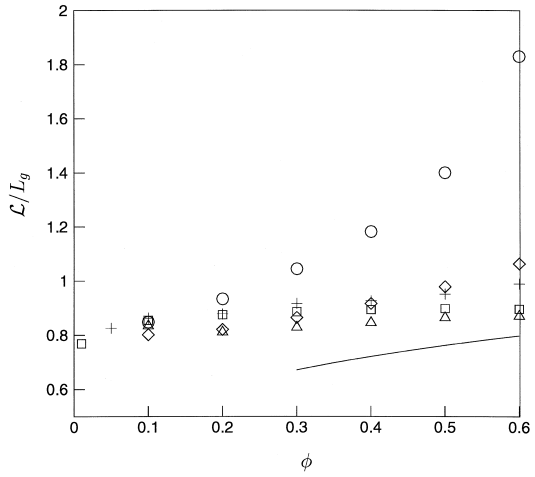

Figure 4. The ratio $\mathcal{L}/L_g$ obtained from fitting the numerical simulation data at each area fraction, as a function of area fraction ϕ. L_g is half the smallest gap size between the cylinders, $((\phi_{\max}/\phi)^{1/2}-1)a$. (□), on-axis transverse flow through square arrays; (Δ), on-axis transverse flow through hexagonal arrays; (◯), longitudinal flow through square arrays; (◊), longitudinal flow through hexagonal arrays; (+), inferred from numerical simulation results for square arrays by Bruschke and Advani [16]. The line corresponds to L/a (numerically integrated over n) obtained from the lubrication theory (15), for transverse flow through square and hexagonal arrays.

law index. This quantity can be shown to be equal to $(L/a)^{-2}$, and we have plotted Bruschke and Advani's results in Figure 4. The agreement with our results is good. Experimental data by Sadiq, Advani and Parnas [35] for the mobility factor showed reasonable agreement with Bruschke and Advani's calculations [16] (the deviations were within 30%). We have not been able to convert the experimental data by Sadiq, Advani and Parnas [35] into drag coefficients because of apparent inconsistencies in their viscosity data. In [14] we do present a comparison with the experimental data of Adams and Bell [36] for flows at finite Reynolds numbers.

Although $\mathcal{L}/a$ hardly shows any dependence on the power-law index, the velocity field varies significantly with n. In Figure 5 we show velocity profiles across the narrowest part of the gap between the cylinders. The shear rate near the cylinder surface is seen to increase strongly with decreasing n, as expected; but the length scale over which the fluid velocity changes in the bulk is the same for all values of n and there is no significant effect on the result for L/a.

4.2. Off-axis transverse flows

For off-axis flows of Newtonian fluids at zero Reynolds number the drag force is aligned with the averaged velocity due to the linearity of the equations of motion and the symmetry of the array. Off-axis, finite-Reynolds-number flows of Newtonian fluids, for which this linearity no longer holds, have been investigated in [4]. The equations of motion for creeping flows of power-law fluids are also nonlinear in the velocity and we do not expect the drag force to align with the averaged velocity vector in this case either. However, the flow field retains the symmetry property ($\mathbf{x} \to -\mathbf{x}$, $\mathbf{v} \to \mathbf{v}$, $P \to -P$) where $\mathbf{x}$ is measured relative to the cylinder centre and P is measured relative to a suitable reference value. This is a generalisation of the fore-aft symmetry for on-axis flows.

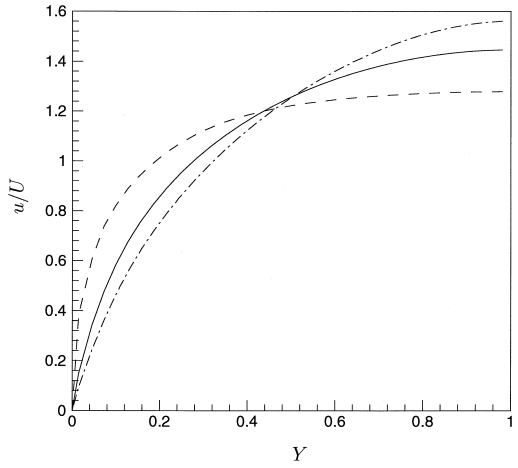

Figure 5. Velocity profile across the narrowest part of the gap for a square array with solid area fraction $\phi = 0{\cdot}01$ and power-law index $n = 0{\cdot}5$ (dashed line), $n = 1$ (solid line) and $n = 1{\cdot}5$ (dash-dotted line). Y is in the surface normal direction and is normalised to half the gap width.

4.2.1. *Lubrication theory for off-axis flows*

The lubrication theory for on-axis flows is generalised to off-axis flows through concentrated arrays by adding the pressure drops over each gap. The lubrication theory shows that the pressure drop through each gap in the array is proportional to the local flux Q to the power n, so that, for square arrays, $F_i \sim \overline{V}_i^n$, where F_i is the i-component of the force on a cylinder in the array [34]. Denoting the angle between the force and the x_1-axis (an axis of the array) by θ_F, and the angle between the averaged velocity and the x_1-axis by θ,

$$\tan\theta = (\tan\theta_F)^{\frac{1}{n}} \qquad (\,|\phi - \phi_{\max}| \ll 1). \tag{17}$$

Thus the averaged velocity of shear-thinning fluids through a concentrated square array is, for large values of ϕ, more aligned with the nearest axis of the array than the drag force is. This is a consequence of the pressure drop over a channel being proportional to the flux to the power n. For the gaps over which the pressure drop is smaller the resulting flow is smaller by a greater factor. Koch and Ladd [4] showed that Newtonian fluids at small-but-finite-Reynolds numbers behave in an opposite manner, and we should expect the same for shear-thickening fluids in creeping flow as is shown by equation (17).

For hexagonal arrays, $F_1 = \sqrt{3}(\Delta p)_1$ and $F_2 = (\Delta p)_2$, and contributions to the pressure drops $(\Delta p)_i$ arise from several gaps (Figure 1b), each being proportional to the appropriate volume flux to the power n. Taking the width of the unit cell in Figure 1b to be unity, assuming that the flow is directed towards the right or towards the upper right corner, and only considering the top half of the unit cell, it follows that,

$$F_2 \sim -\left(\frac{1}{2}\sqrt{3}\,\overline{V}_1 - \frac{1}{2}\overline{V}_2\right)^n + \left(\frac{1}{2}\sqrt{3}\,\overline{V}_1 + \frac{1}{2}\overline{V}_2\right)^n + \overline{V}_2^n, \tag{18}$$

as well as a similar expression for F_1, with the same proportionality factor. It is convenient to normalise the tangents of θ and θ_F with $1/\sqrt{3}$, *i.e.*, the tangent of the symmetry angle. Using the notation $\mu \equiv \sqrt{3}\tan\theta$ and $\mu_F \equiv \sqrt{3}\tan\theta_F$, we find,

$$\mu_F = \frac{(3+\mu)^n - (3-\mu)^n + 2(2\mu)^n}{(3+\mu)^n + (3-\mu)^n} \qquad (\,|\phi - \phi_{\max}| \ll 1). \tag{19}$$

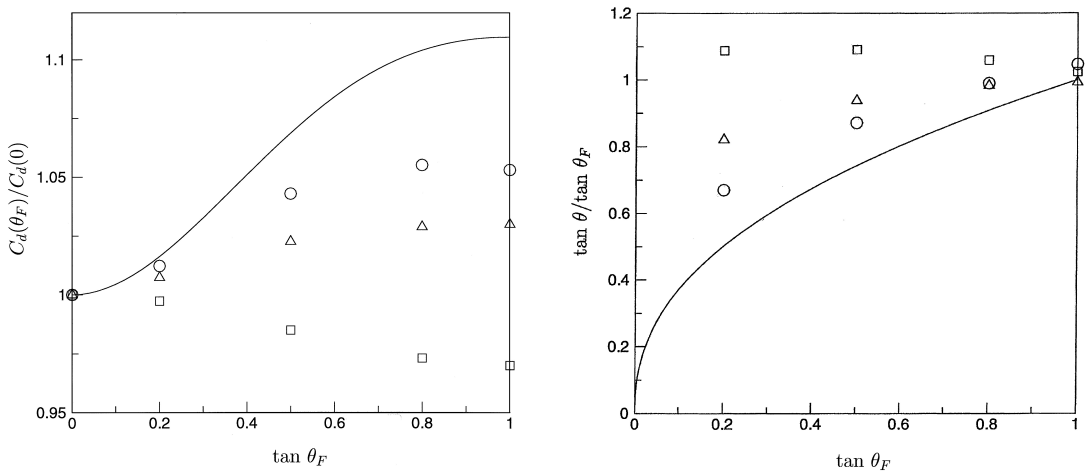

Figure 6. The ratio of the drag coefficient for off-axis transverse flow through square arrays to the on-axis drag coefficient (*a*) and the ratio of the tangent of the angle θ that the averaged velocity makes with the nearest axis of the array and the tangent of the angle θ_F that the applied pressure drop over the array makes with the nearest axis of the array (*b*), as functions of the tangent of the angle θ_F for $n = 0.7$ at different area fractions: (□), $\phi = 0{\cdot}1$; (△), $\phi = 0{\cdot}3$; (◯), $\phi = 0{\cdot}5$. The lines are the lubrication results (20) and (17).

The drag coefficient for off-axis flows is defined by (14). From $F = |\mathbf{F}|$, $U = |\overline{\mathbf{V}}|$, and using (17), we obtain $C_d(\theta_F) \sim (\overline{V}_1^{2n} + \overline{V}_2^{2n})^{1/2}/(\overline{V}_1^2 + \overline{V}_2^2)^{n/2}$. The magnitude of the force is therefore related to that for on-axis flows for concentrated square arrays by,

$$\frac{C_d(\theta_F)}{C_d(0)} = \frac{\left(1 + (\tan\theta_F)^2\right)^{1/2}}{\left(1 + (\tan\theta_F)^{2/n}\right)^{n/2}} \qquad (|\phi - \phi_{\max}| \ll 1). \tag{20}$$

The drag coefficient for off-axis flow through hexagonal arrays is obtained similarly, resulting in,

$$\frac{C_d(\mu_F)}{C_d(0)} = \frac{\left(9 + 3\mu^2\right)^{-n/2}}{2\sqrt{3}} \left\{3\left[(3+\mu)^n + (3-\mu)^n\right]^2 + \left[(3+\mu)^n - (3-\mu)^n + 2\,(2\mu)^n\right]^2\right\}^{1/2}, \tag{21}$$

which is written in terms of θ rather than θ_F, for convenience. Both expressions show a gradual increase of the drag coefficient with increasing θ, up to the corresponding symmetry angle.

4.2.2. *Numerical results for off-axis flows*

In Figure 6a the drag force coefficient ratio $C_d(\theta_F)/C_d(0)$ is shown for square arrays at $n = 0{\cdot}7$ and $\phi = 0{\cdot}1$, $0{\cdot}3$ and $0{\cdot}5$ as a function of tan θ_F; the ratio tan θ/tan θ_F is shown as a function of tan θ_F for the same area fractions in Figure 6b. The drag force is seen to be almost aligned with the averaged velocity at low area fractions (the velocity makes a somewhat larger angle than the drag force with the nearest axis of the array), and to gradually decrease in magnitude for off-axis flows. For higher area fractions, the opposite is true, the force increases for off-axis flows and is less aligned with the nearest axis of the array than is the averaged

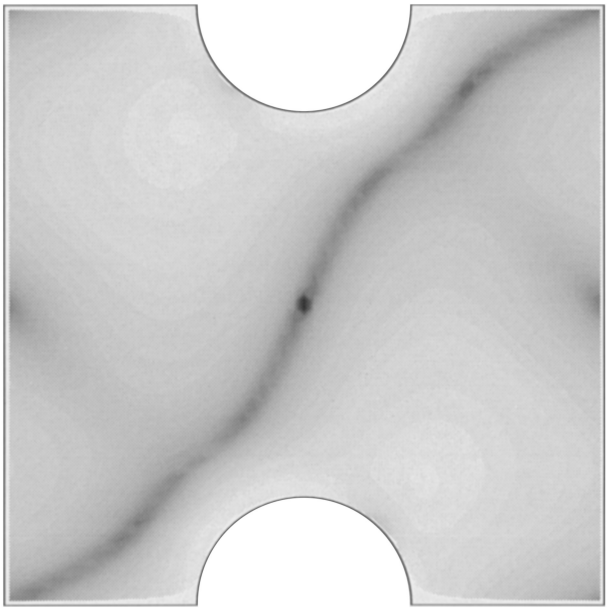

Figure 7. Fluid viscosity field for off-axis flow of a power-law fluid ($n = 0{\cdot}7$) through a square array at solid area fraction $\phi = 0{\cdot}1$ with $\tan\theta_F = 1$. Dark regions correspond to large viscosity values.

velocity. The results are seen to approach the lubrication expressions (17) and (20) for high area fractions. The corresponding results have been computed for hexagonal arrays, these are similar to those for square arrays, with the difference that the drag coefficient increases slightly with θ_F, for all values of ϕ considered. Also, the drag force is always less aligned with the nearest axis of the array than is the averaged velocity. At zero area fraction the drag coefficient should be independent of flow direction. When the area fraction value is decreased from $0{\cdot}3$ to $0{\cdot}1$ the drag coefficient undershoots this limit for square arrays, becoming smaller than for on-axis flows; no similar trend occurs in hexagonal arrays.

In Figure 7 the local viscosity is shown for power-law fluid flow ($n = 0{\cdot}7$) at an angle of 45° with $\phi = 0{\cdot}1$; we see that a 'plug-flow' region of very high viscosity has formed around the 45° axis. This region is much smaller for on-axis flows, and hence the drag coefficient is smaller for off-axis flows. Furthermore, for slightly off-axis flows the formation of the plug-flow region leads to the averaged fluid velocity being aligned more with the 45° axis, which explains why at $\phi = 0{\cdot}1$ the fluid velocity makes a larger angle with the nearest axis of the array than the drag force.

The main trend in the results is simply the approach towards the lubrication theory result as ϕ is increased. Although the creeping flows of power-law fluids are not related to flows of Newtonian fluids at moderate Reynolds numbers ($\mathrm{Re} > 50$), Koch and Ladd [4] found very similar results for the latter: the magnitude of the drag increased whereas the averaged velocity tended to align with one of the axes of the array. They demonstrated that the horizontal velocity component was larger below than above the cylinder, which, together with a slight asymmetry in the wake, caused a significant vertical drag (lift) force component whereas the averaged velocity was almost aligned with the horizontal axis. As in the current work, it was found that it is generally more difficult to force fluid through an array in a direction other than an axis of the array.

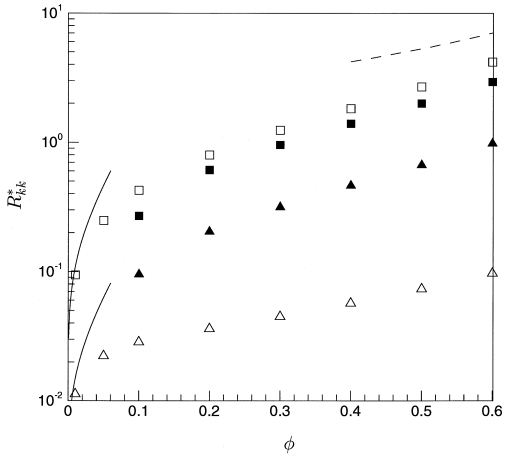

Figure 8. Dimensionless velocity variance components R^*_{kk} for on-axis Newtonian flows through square arrays (open symbols) and hexagonal arrays (filled symbols), as functions of the solid area fraction ϕ. (□), R^*_{11}; (△), R^*_{22}. The solid lines indicate the dilute theory (28), the dashed line is the lubrication theory (23).

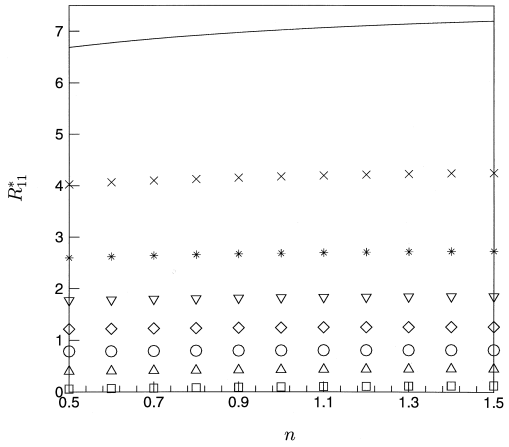

Figure 9. Dimensionless velocity variance component in the direction of the mean flow R^*_{11} for on-axis flows of power-law fluids through square arrays as functions of power-law index n at solid area fractions $\phi = 0{\cdot}01$ (□), $0{\cdot}1$ (△), $0{\cdot}2$ (◯), $0{\cdot}3$ (◇), $0{\cdot}4$ (▽), $0{\cdot}5$ (∗) and $0{\cdot}6$ (×). The line is the lubrication theory (23) for the square array with solid area fraction $\phi = 0{\cdot}6$.

5. Velocity variances

5.1. On-axis transverse and longitudinal flows

The velocity variance tensor for on-axis flow (in the x_1-direction) through a periodic array is written as,

$$\overline{v_i v_j} \equiv \overline{(V_i - \overline{V}_i)(V_j - \overline{V}_j)} \equiv R^*_{ij}(\phi, n)\, \overline{V}_1{}^2, \tag{22}$$

where an overbar denotes the average over the unit cell. Very little is known about the velocity variance in periodic arrays, even for Newtonian fluids. Traditionally, the Reynolds number of the macroscale flow is assumed to be small as well as that for the microscale. Also, the velocity variances could be neglected in the development of analytical results for the drag coefficient in the dilute limit [21]. Recently, however, results have been presented for velocity variances for periodic arrays of spheres [22] and for random arrays of cylinders [37]. We test here whether our results for the velocity variances are consistent with the simple scaling obtained for the drag coefficient (and hence, for the cell-averaged velocity), which suggests that the velocity variances do not depend significantly on the power-law index. The velocity variances are also required for the description of unsteady flows in Section 8 below.

The velocity variance component R^*_{11} for on-axis flows of Newtonian fluids through square and hexagonal arrays is shown in Figure 8 as a function of area fraction. Since the fluid is greatly accelerated as it passes through the narrow gap between the cylinders at high area fractions the velocity variances strongly increase with area fraction. A lubrication theory for R^*_{11} for square arrays is also shown. At high area fractions the main contribution to the cell-average of V_1^2 comes from the narrow gap between the cylinders. This does not hold for V_2^2, so

that a lubrication approximation for R_{22}^* can not be obtained. In the gap, V_1^2 is of $O(U^2/\varepsilon^2)$; the gap size is of $O(a^2\varepsilon^{3/2})$, so that the integrated square of the velocity is of $O(U^2a^2/\varepsilon^{1/2})$. Therefore, R_{11}^* is of $O(\varepsilon^{-1/2})$. The exact expression is, for square arrays,

$$R_{11}^* = \frac{\sqrt{2}\,\pi(1+2n)}{2+3n}\left(\frac{\phi}{\phi_{\max}}\right)^{1/4}\left(1-\left(\frac{\phi}{\phi_{\max}}\right)^{1/2}\right)^{-1/2} \qquad (|\phi-\phi_{\max}| \ll 1). \tag{23}$$

This result has been plotted together with the numerical results in Figure 8. The lubrication approximation for the velocity variances becomes valid only at very high area fractions because it decreases only with the inverse square root of the gap size whereas for the drag coefficient lubrication theory the pressure gradient is integrated, which decreases with the gap size to the power $-2n-1/2$. The lubrication theory for R_{ij}^* for the hexagonal array was found to be applicable only at area fractions that are even higher. The result for hexagonal arrays is

$$R_{22}^* = \frac{1}{3}R_{11}^*, \quad R_{11}^* = \frac{(3/2)^{3/2}\pi(1+2n)}{2+3n}\left(\frac{\phi}{\phi_{\max}}\right)^{1/4}\left(1-\left(\frac{\phi}{\phi_{\max}}\right)^{1/2}\right)^{-1/2} \tag{24}$$

$(|\phi-\phi_{\max}| \ll 1)$.

It is interesting that the ratio R_{22}^*/R_{11}^* remains close to $1/3$ even for modest values of ϕ.

For flows of Newtonian fluids through dilute arrays the exact solution can be used in the point-force approximation [38] to obtain an explicit result for the velocity variances. The velocity disturbance generated by the cylinders is,

$$\mathbf{v}(\mathbf{x}) = \sum_{k\neq 0}\hat{\mathbf{v}}(\mathbf{k})\exp\left(-2\pi i\mathbf{k}\cdot\mathbf{x}\right), \tag{25}$$

where $\mathbf{k}$ is the wavenumber vector made dimensionless with the distance between neighbouring cylinder centres, $k = |\mathbf{k}|$ and,

$$\hat{\mathbf{v}}(\mathbf{k}) = -\frac{\mathbf{F}\cdot\left(\mathbf{I}-\mathbf{kk}/k^2\right)}{\mu(2\pi k)^2}. \tag{26}$$

The force on a cylinder in a dilute square periodic array for Newtonian fluids has been calculated by Hasimoto [38] and Sangani and Acrivos [1],

$$F = 4\pi\mu U\left(\log\,\phi^{-1/2} - 0{\cdot}738 + O(\phi)\right)^{-1} \qquad (\phi \ll 1). \tag{27}$$

Integrating disturbance velocity products over the unit cell yields single summations over wavenumber space [22]. We determined these summations numerically, and the final results for the dimensionless velocity variance components are, for square arrays,

$$R_{22}^* = 0{\cdot}135R_{11}^*, \quad R_{11}^* = 0{\cdot}269\left(\log\,\phi^{-1/2} - 0{\cdot}738 + O(\phi)\right)^{-2} \qquad (\phi \ll 1). \tag{28}$$

From Figure 8 we see that the numerical simulation data for $\phi = 0{\cdot}01$ are in agreement with these asymptotic results.

Figure 9 shows R_{11}^* for on-axis flows through square arrays, plotted against the power-law index n at different area fractions. Also shown is the lubrication approximation (23) for the square array with $\phi = 0{\cdot}6$. The results for hexagonal arrays, and for R_{33}^* in longitudinal

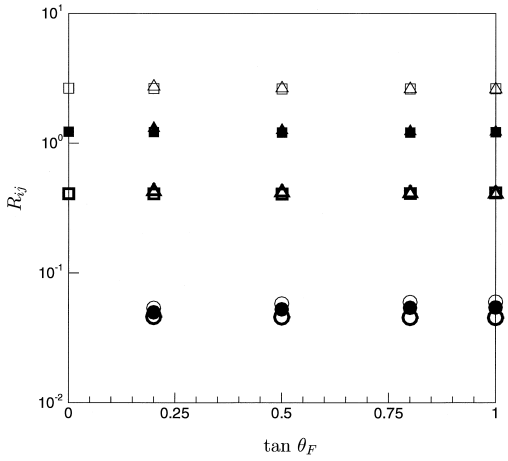

Figure 10. Dimensionless velocity variance components for off-axis flow through square arrays as functions of the angle θ_F that the drag force makes with an axis of the array. Squares are R_{11}, triangles are R_{22} and circles are R_{12}. Open symbols are for solid area fraction $\phi = 0{\cdot}5$, filled symbols are $\phi = 0{\cdot}3$ and boldface open symbols are $\phi = 0{\cdot}1$. The power-law index is $n = 0{\cdot}7$.

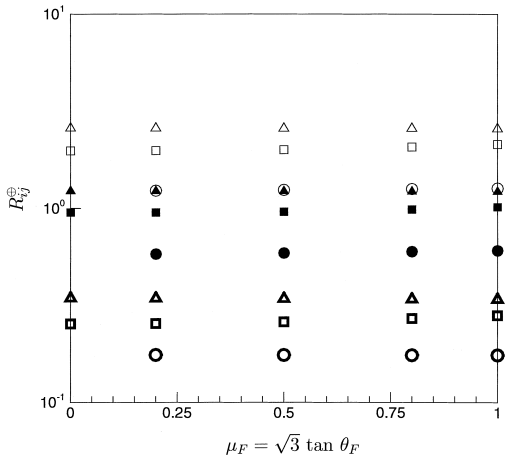

Figure 11. Dimensionless velocity variance components for off-axis flow through hexagonal arrays as functions of the angle θ_F that the drag force makes with an axis of the array. Squares are $R^{\oplus}_{11}$, triangles are $R^{\oplus}_{kk}$ and circles are $R^{\oplus}_{12}$. Open symbols are for solid area fraction $\phi = 0{\cdot}5$, filled symbols are $\phi = 0{\cdot}3$ and boldface open symbols are $\phi = 0{\cdot}1$. The power-law index is $n = 0{\cdot}7$.

flows through square arrays, are very similar to the results for the transverse flow case and are therefore not reproduced here. The velocity variance is seen to be only weakly dependent on n at all area fractions. Also, the dependence of R^*_{11} on n was found to be of the same order as that of R^*_{22}, which is much smaller in magnitude: the changes in the structure of the velocity field with power-law index are not sufficient to alter the velocity variances. This is consistent with the results presented in the previous section for the drag coefficient (which is related to the averaged velocity, the first moment of the velocity vector field), which was found to obey a simple scaling relation.

5.2. Off-axis transverse flows

The definition (22) is generalised for off-axis transverse flows in the form,

$$\overline{v_i v_j} \equiv \overline{(V_i - \overline{V}_i)(V_j - \overline{V}_j)} \equiv R_{ij}(\phi, n, \theta)\overline{V}_i\overline{V}_j + R^*_{22}(\phi, n)\left(\overline{V}_2{}^2\delta_{i1}\delta_{j1} + \overline{V}_1{}^2\delta_{i2}\delta_{j2}\right), \quad (29)$$

where no summation over i and j is presumed. This new definition is expected to give the smallest dependence of R_{ij} on the angle between the drag force and an axis of the array. The last terms on the right-hand side account for the finite value of R^*_{22} for on-axis flows.

In Figure 10 the three components of the velocity variance tensor are shown as functions of $\tan\theta_F$ at several area fractions for flows of shear-thinning fluids ($n = 0{\cdot}7$) through square arrays. It is seen that R_{12} is an order of magnitude smaller than the normal velocity variances, indicating a decorrelation between the velocity components. From symmetry arguments we expect that R_{22} is equal to R_{11} for all ϕ at $\tan\theta_F = 1$, which is confirmed by Figure 10. None of the components of R_{ij} show a significant dependence on the angle the force makes with the

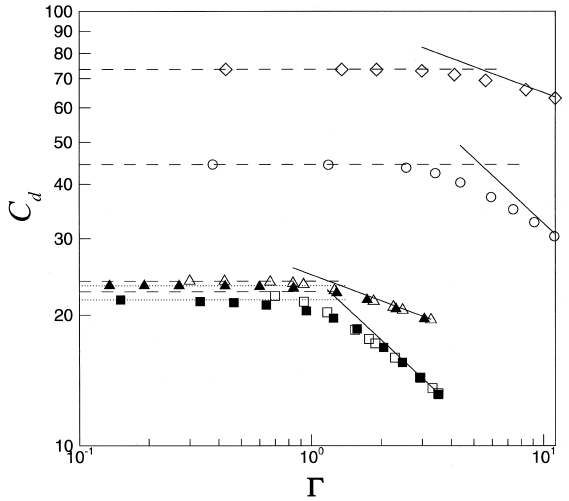

Figure 12. Drag coefficient for a cylinder in a square array as function of the dimensionless transition shear rate $\Gamma = \dot{\gamma}_0 a/U$. (□), $\phi = 0{\cdot}1$, $n = 0{\cdot}5$; (△), $\phi = 0{\cdot}1$, $n = 0{\cdot}8$; (◯), $\phi = 0{\cdot}3$, $n = 0{\cdot}5$; (◇), $\phi = 0{\cdot}3$, $n = 0{\cdot}8$. Open symbols are for on-axis flow, filled symbols for off-axis flow with $\theta = 45°$. The solid lines indicate the Newtonian result (30) at large Γ and the dashed lines are the asymptotic power-law fluid result at small Γ, all for on-axis flows. The dotted lines indicate the asymptotic power-law fluid results for off-axis flows.

axes of the array. Hence $R_{22} \approx R_{11} \approx R_{11}^*$ (which showed no significant dependence on the power-law index).

Results for the velocity variances for off-axis flows through hexagonal arrays are shown in Figure 11, for the normal component along one of the axes of the array $R_{11}^{\oplus} \equiv \overline{v_1^2}/\overline{V}_1^2$, the trace $R_{kk}^{\oplus} \equiv \overline{v_k v_k}/|\overline{\mathbf{V}}|^2$ and the off-diagonal component $R_{12}^{\oplus} \equiv \overline{v_1 v_2}/(\overline{V}_1 \overline{V}_2)$. No significant flow-angle dependence is seen, so that simply on-axis flow values can be used for the normal velocity variances.

6. Effect of low-shear Newtonian regions

The results presented so far are for the limiting case of power-law fluids: in (5), the low-shear Newtonian plateau is reached only in small regions of the flow that do not affect the results. The effect on the results of changing the onset of the Newtonian plateau is now addressed.

In Figure 12 we show results for the drag coefficient of a cylinder in a square array as a function of the dimensionless parameter $\Gamma = \dot{\gamma}_0 a/U$ for $n = 0{\cdot}5$ and $0{\cdot}8$ with solid area fraction $0{\cdot}1$ and $0{\cdot}3$. The results for off-axis flow ($\theta = 45°$) are seen to be similar to the on-axis results. For small values of Γ the drag coefficient and velocity variances will converge to the results presented above for the power-law limit. At large enough values of Γ the shear rates in the entire domain are not sufficient for the fluid to depart from the Newtonian behaviour, resulting in,

$$C_d(\phi, n, \Gamma) = \Gamma^{1-n} C_d(\phi, n = 1, \Gamma \to \infty) \qquad (\Gamma \ll 1). \tag{30}$$

We see from Figure 12 that the numerical simulation results simply exhibit a smooth transition between the two asymptotic cases. A good approximation for a critical value Γ_c, at which the low-shear Newtonian plateau causes a significant change from the power-law results presented

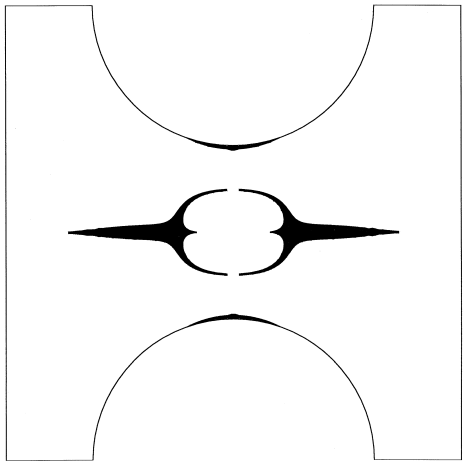

Figure 13. The distribution of the ratio X defined by (33), indicating the areas where elongation is important. The dark regions correspond to low values of X. Solid fraction $\phi = 0{\cdot}3$, power-law index $n = 0{\cdot}8$.

above, can thus be obtained simply from the point of intersection of the two asymptotes, *i.e.*,

$$\Gamma_c = (C_d(\phi, n)/C_d(\phi, 1))^{1/(1-n)} = \left(\frac{\phi}{\phi_{\max}}\right)^{1/2} \left(\frac{\mathcal{L}}{a}\right)^2, \tag{31}$$

where we have used (16). Alternatively, in the definition of Γ_c a shear rate other than U/a could have been used to absorb the right-hand side of (31). We note that this estimate of Γ_c is independent of the value of the power-law index n and that Γ_c is $O(1)$ only for low area fractions, and increases with ϕ. The results presented above for the power-law fluid limit are therefore applicable for a wide range of flows involving fluids whose behaviour can be approximated with the truncated power-law model. A departure from the power-law fluid result occurs only for a very low pressure drop across the array.

From the results presented in Section 5 it is clear that the two limiting cases for the velocity variances (power-law at small Γ, Newtonian at large Γ) yield virtually identical values, and our simulation results for intermediate values of Γ indicate that the power-law fluid results presented above can be used for any value of Γ.

7. Extensional viscosity

In the truncated power-law fluid model no effect of extensional thickening is accounted for. However, previous work [12, 11] suggests that, despite the diverging/contracting geometry of periodic arrays of cylinders, the flow in these geometries is dominated by shear, not extension. In this section we investigate the cause of the dominance of shear.

A model that combines truncated power-law shear viscosity with extensional thickening was proposed by Schunk and Scriven [39]. The local viscosity is a weighted average of the truncated power-law shear viscosity and the extensional-thickening viscosity. The weight factor is an indicator of the importance of the rate of rotation of the fluid with respect to the principal axes of the rate-of-strain tensor, and the magnitude of rate-of-strain tensor. If the fluid rotates rapidly with respect to the principal axes of the rate-of-strain tensor, a fluid particle will not be elongated significantly and the viscosity becomes equal to the shear viscosity. In

regions of large strain rate or low relative rotation the elongation is large and the fluid viscosity increases.

Denoting the ith principal axis of the rate-of-strain tensor by $\mathbf{e}^i$, its relative rotation with respect to a fluid particle is,

$$\mathbf{W}_{\text{rel}} = \mathbf{e}^i \times \left(\frac{\partial \mathbf{e}^i}{\partial t} + \mathbf{V} \cdot \nabla \mathbf{e}^i \right) - \frac{1}{2} \nabla \times \mathbf{V}. \tag{32}$$

A measure of the rate-of-strain is the second invariant Π, and the rate of relative rotation compared to the magnitude of the rate of strain is,

$$X = |\mathbf{W}_{\text{rel}}| \, / \, \Pi. \tag{33}$$

Effects of elongation are expected to be large in areas where X is less than unity [39].

In accordance with the model of Schunk and Scriven [39], we have used a Carreau-type shear viscosity in this case,

$$\eta = \eta_\infty - (\eta_\infty - \eta_0) \, (1 + \lambda \Pi)^{(n-1)/2} \, . \tag{34}$$

In Schunk and Scriven's model an analogous expression for the extensional viscosity is used, and the total local viscosity is a weighted average of both viscosities, the weight factor being a function of X.

In Figure 13 the areas where $X < 1$ are shown for $n = 0{\cdot}8$ and solid fraction $\phi = 0{\cdot}3$; other cases yielded very similar results. We found that X is not much affected by a difference between shear and extensional viscosities, so we have used (34) here as the total local viscosity. X is seen to be smaller than unity only for a narrow band around the plane of symmetry and a ring around the centre of the domain. The ring coincides with the place where the transition occurs between the low-shear Newtonian plateau and the power-law range in the shear viscosity. We saw in the previous section that the area around the plane of symmetry does not contribute significantly to the results. In most of the rest of the domain the flow is dominated by the effects of shear. In the thin areas of $X < 1$ just above and below the cylinders X becomes small not because of large strain but because large shear makes Π larger than $|\mathbf{W}_{\text{rel}}|$.

The results for low solid fraction are very similar; the area around the symmetry plane where $X < 1$ does not grow. Of course, the rate of extension is already small in that case. For the more concentrated arrays, the streamlines are not very curved: because of the existence of recirculation zones between the cylinders the flow is similar to a channel flow. A case where extension could be very important is the flow through a first (or single) row of cylinders rather than an infinite periodic array, similar to the flow through a contraction for which extension is known to be important [40, 41].

8. Time-dependent flows

We now investigate whether it is possible to approximate the drag force in unsteady flows from the steady state results presented above, following an argument developed by Hill, Koch and Ladd [22] for Newtonian fluid flows through fixed arrays of spheres. For a uniform bed, with a constant pressure gradient turned on at $t = 0$, equation (1) becomes,

$$\rho \frac{\mathrm{d}\overline{V}}{\mathrm{d}t} = \frac{\phi}{\pi a^2} \, (F_\infty - F) \, , \tag{35}$$

where F and F_∞ are the time-dependent and steady-state force (per unit cylinder length) exerted on a cylinder, respectively (F_∞ represents the driving pressure gradient in the bed). A general approximation for the time-dependent force on a cylinder is,

$$F = C_d K a^{1-n} \overline{V}^n + (1 + C_a)\pi a^2 \frac{\mathrm{d}\overline{V}}{\mathrm{d}t}, \tag{36}$$

where C_a is the added mass coefficient. The second term on the right-hand side is the acceleration reaction or added mass force. The history force is generally dominated by either the quasi-steady drag or the inertia term in (36) and represents a small correction to (36) [42]. After substituting (36) in (35) and rearranging, we have

$$\frac{\mathrm{d}\overline{V}_*}{\mathrm{d}t_*} = \mathrm{St}^{-1}\left(1 - \overline{V}_*^n\right), \tag{37}$$

where $\overline{V}_* = \overline{V}/V_\infty$ (V_∞ is the steady-state cell-averaged fluid velocity), $t_* = t\rho^{-1}Ka^{-1-n}V_\infty^{n-1}$ and

$$\mathrm{St} = \pi(1 + \phi(1 + C_a))/C_d, \tag{38}$$

is an effective Stokes number. The time-dependent force acting on a cylinder can be obtained from substituting the solution of (37) into (36).

Hill, Koch and Ladd [22] showed recently that for long time periods, as the (Newtonian fluid) flow converges to the steady state solution, the added mass coefficient of a sphere in a periodic array can be obtained from a simplified energy balance. By assuming at long times that the flow is quasi-steady, the time rate of change of kinetic energy in a frame moving with the averaged velocity can be equated to the rate of work done by the quasi-steady drag force, Hill, Koch and Ladd [22] showed that the added mass coefficient is related to the dimensionless velocity variances through

$$C_a = R_{kk}/\phi - 1. \tag{39}$$

In Figure 14 we present some examples showing how well the solution of (37) with (38–39) agrees with our numerical simulation data, even for relatively short times. In Figure 15, values of St obtained by fitting (37) to the simulation data are shown. The lines indicate the analytical result (38–39), where we have used (16) and the velocity variance R_{kk} averaged over the power-law index n. The quasi-steady theory is seen to be in excellent agreement for a range of power-law index and solid fraction. The slight deviation at low n is due to the approximations used for R_{kk}.

9. Conclusions

Numerical results have been presented together with lubrication theories for the flow of truncated power-law fluids through square and hexagonal arrays, both off-axis transverse flows and longitudinal flows. The strong dependence of the steady-state drag coefficient on the power-law index was shown to be caused by the choice of velocity and length scale in the definition of the drag coefficient. Comparison between velocity profiles for different power-law index (n) values confirm that the typical length scale of the flow is approximately independent of n. Hence, the drag coefficient defined by (14) can be approximated by (16), with

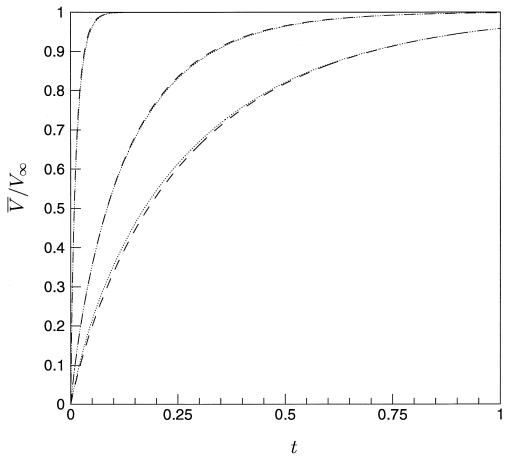

Figure 14. Cell-averaged fluid velocity $\overline{V}$ divided by its steady-state value V_∞ from numerical simulations for on-axis flow through a square array started from rest (dotted lines) and the theory (37–39) (dashed lines) for $n = 0{\cdot}5$ and, from right to left, $\phi = 0{\cdot}1$, $0{\cdot}2$ and $0{\cdot}5$.

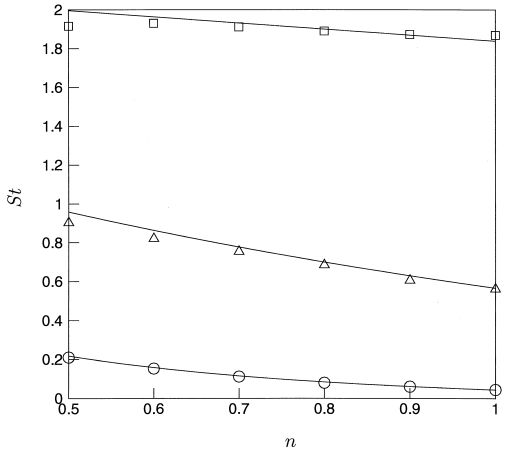

Figure 15. Effective Stokes number for transient on-axis flows through square arrays as a function of power-law index n, obtained from fitting the numerical solution of (37) to the full numerical simulation data for $\phi = 0{\cdot}1$ (□), $\phi = 0{\cdot}2$ (Δ) and $\phi = 0{\cdot}5$ (◯). The lines are the quasi-steady theory (38–39), where C_d was obtained from (16) and the n-averaged values of R_{kk} were used.

L/a replaced by $\mathcal{L}/a$. $\mathcal{L}/a$ can be inferred from Figure 4 for a range of geometries, and depends only on the solid area fraction ϕ and the geometry of the array.

For off-axis flows of shear-thinning fluids the drag force was shown to be generally less aligned with the nearest axis of the array than the averaged velocity: due to the nonlinear dependence of the drag on the fluid velocity, it is more difficult to force power-law fluids through an array in a direction other than an axis of the array. The low-shear Newtonian behaviour of the fluid only affects the results for very low flow rates, and then in a straightforward manner. Elongation was shown to be important only in areas around the axis of symmetry; elsewhere the flow is dominated by shear effects. The steady-state results for the drag coefficient and velocity variances have been used to predict the transient behaviour as the fluid is accelerated from rest.

The finding that for creeping flows of power-law fluids through arrays of circular cylinders the drag can be scaled to become virtually independent of the power-law index is useful for the understanding of other inelastic non-Newtonian fluid flows. In a companion paper [14], we present results for the corresponding flows with finite inertia and show that simple scaling arguments can be used for the correction to the drag coefficient due to finite Reynolds numbers. In [34] we show that results for creeping flows of power-law fluids through arrays of elliptical cylinders follow similar trends to those presented here.

Acknowledgements

This work has been made possible by a grant from the EPSRC (GR/M 39572) and has been supported by QinetiQ, Vosper Thornycroft, Dowty Aerospace Propellers, AEA Technology

and BAE Systems. We would like to thank Mr. Li Ding and Prof. Robert L. Street of Stanford University for valuable suggestions on details of the implementation of the numerical method. The authors gratefully acknowledge the computer facilities provided under EPSRC grant GR/L86821.

References

1. A.S. Sangani and A. Acrivos, Slow flow past periodic arrays of cylinders with application to heat transfer. *Int. J. Multiphase Flow* 8 (1982) 193–206.
2. J.E. Drummond and M.I. Tahir, Laminar viscous flow through regular arrays of parallel solid cylinders. *Int. J. Multiphase Flow* 10 (1984) 515–540.
3. A.S. Sangani and C. Yao, Transport processes in random arrays of cylinders. II. Viscous flow. *Phys. Fluids* 31 (1988) 2435–2444.
4. D.L. Koch and A.J.C. Ladd, Moderate Reynolds number flows through periodic and random arrays of aligned cylinders. *J. Fluid Mech.* 349 (1997) 31–66.
5. C. Chmielewski, C.A. Petty and K. Jayaraman, Crossflow of elastic liquids through arrays of cylinders. *J. Non-Newt. Fluid Mech.* 35 (1990) 309–325.
6. J. Vorwerk and P.O. Brunn, Porous medium flow of the fluid A1: effects of shear and elongation. *J. Non-Newt. Fluid Mech.* 41 (1991) 119–131.
7. L. Skartsis, B. Khomami and J.L. Kardos, Polymeric flow through fibrous media. *J. Rheol.* 36 (1992) 589–620.
8. C. Chmielewski, and K. Jayaraman, Elastic instability in crossflow of polymer solutions through periodic arrays of cylinders. *J. Non-Newt. Fluid Mech.* 48 (1993) 285–301.
9. B. Khomami and L.D. Moreno, Stability of viscoelastic flow around periodic arrays of cylinders. *Rheol. Acta* 36 (1997) 367–383.
10. G.K. Batchelor, The stress generated in a non-dilute suspension of elongated particles by pure straining motion. *J. Fluid Mech.* 46 (1971) 813–829.
11. K.K. Talwar and B. Khomami, Flow of viscoelastic fluids past periodic square arrays of cylinders: inertial and shear thinning viscosity and elasticity effects. *J. Non-Newt. Fluid Mech.* 57 (1995) 177–202.
12. A.W. Liu, D.E. Bornside, R.C. Armstrong and R.A. Brown, Viscoelastic flow of polymer solutions around a periodic, linear array of cylinders: comparisons of predictions for microstructure and flow fields. *J. Non-Newt. Fluid Mech.* 77 (1998) 153–190.
13. R.B. Bird, R.C. Armstrong, and O. Hassager, *Dynamics of Polymeric Liquids. Vol. 1: Fluid Mechanics.* New York: John Wiley (1987) 649 pp.
14. P.D.M. Spelt, T. Selerland, C.J. Lawrence and P.D. Lee, Flows of inelastic non-Newtonian fluids through arrays of aligned cylinders. Part 2. Inertial effects for square arrays. Submitted to *J. Eng. Math.* (2005) 81–97.
15. R.I. Tanner, Stokes paradox for power-law flow around a cylinder. *J. Non-Newt. Fluid Mech.* 50 (1993) 217–224.
16. M.V. Bruschke and S.G. Advani, Flow of generalized Newtonian fluids across a periodic array of cylinders. *J. Rheol.* 37 (1993) 479–498.
17. S.J.D. D'Alessio, and J.P. Pascal, Steady flow of a power-law fluid past a cylinder. *Acta Mech.* 117 (1996) 87–100.
18. M. Vijaysri, R.P. Chhabra and V. Eswaran, Power-law fluid flow across an array of infinite circular cylinders: a numerical study. *J. Non-Newt. Fluid Mech.* 87 (1999) 263–282.
19. C.B. Shah and Y.C. Yortsos, Aspects of flow of power-law fluids in porous media. *AIChE J.* 41 (1995) 1099–1112.
20. J.R.A. Pearson and P.M.J. Tardy, Models for flow of non-Newtonian and complex fluids through porous media. *J. Non-Newt. Fluid Mech.* 102 (2002) 447–473.
21. E.J. Hinch, An averaged-equation approach to particle interactions in a fluid suspension. *J. Fluid Mech.* 83 (1977) 695–720.
22. R.J. Hill, D.L. Koch and A.J.C. Ladd, The first effects of fluid inertia on flows in ordered and random arrays of spheres. *J. Fluid Mech.* 448 (2001) 213–241.

23. A.J.C. Ladd, Hydrodynamic transport coefficients of random dispersions of hard spheres.*J. Chem. Phys.* 93 (1990) 3484–3494.
24. G. Mo, and A.S. Sangani, A method for computing Stokes flow interactions among spherical objects and its application to spherical drops and porous particles. *Phys. Fluids* 6 (1994) 1637–1652.
25. N. Martys, D.P. Bentz and E.J. Garboczi, Computer simulation study of the effective viscosity in Brinkman's equation. *Phys. Fluids* 6 (1994) 1434–1439.
26. S.K. Gupte, S.K. and S.G. Advani, Flow near the permeable boundary of an aligned fibre preform: an experimental investigation using laser doppler anemometry. *Polym. Comp.* 18 (1997) 114–124.
27. C.D. Tsakiroglou, A methodology for the derivation of non-Darcian models for the flow of generalized Newtonian fluids in porous media. *J. Non-Newt. Fluid Mech.* 105 (2002) 79–110.
28. W.B. Russel, D.A. Saville and W.R. Schowalter, *Colloidal Dispersions.* Cambridge: Cambridge University Press (1989) 525 pp.
29. Y. Zang, R.L. Street and J.R. Koseff, A non-staggered grid, fractional step method for time-dependent incompressible Navier-Stokes equations in curvilinear coordinates. *J. Comp. Phys.* 114 (1994) 18–33.
30. Y. Zang and R.L. Street, A composite multigrid method for calculating unsteady incompressible flows in geometrically complex domains. *Int. J. Num. Meth. Fluids* 20 (1995) 341–361.
31. L.L. Yuan, R.L. Street and J.H. Ferziger, Large-eddy simulations of a round jet in crossflow. *J. Fluid Mech.* 379 (1999) 71–104.
32. H.F. Bulthuis, *Dynamics of Bubbly Flows*. Ph.D. thesis, University of Twente, the Netherlands (1997) 132 pp.
33. A. Iafrati, A. Di Mascio and E.F. Campana, A level set technique applied to unsteady free surface flows. *Int. J. Num. Meth. Fluids* 35 (2001) 281–297.
34. J.K. Woods, P.D.M. Spelt , T. Selerland, C.J. Lawrence and P.D. Lee, Creeping flows of power-law fluids through periodic arrays of elliptical cylinders. *J. Non-Newt. Fluid Mech.* 111 (2003) 211–228.
35. T.A.K. Sadiq, S.G. Advani and R.S. Parnas, Experimental investigation of transverse flow through aligned cylinders. *Int. J. Multiphase Flow* 21 (1995) 755–774.
36. D. Adams and K.J. Bell, Fluid friction and heat transfer for flow of sodium carboxy methylcellulose solutions across banks of tubes. *Chem. Eng. Prog. Symp. Ser.* 64 (1968) 133–145.
37. D.L. Koch, R.J. Hill and A.S. Sangani, Brinkman screening and the covariance of the fluid velocity in fixed beds. *Phys. Fluids* 10 (1998) 3035–3037.
38. H. Hasimoto, On the periodic fundamental solutions of the Stokes equations and their application to viscous flow past a cubic array of spheres. *J. Fluid Mech.* 5 (1959) 317–328.
39. P.R. Schunk and L.E. Scriven, Constitutive equation for modeling mixed extension and shear in polymer solution processing. *J. Rheol.* 34 (1990) 1085–1119.
40. A.M. Wunderlich, P.O. Brunn and F. Durst, Flow of dilute polyacrylamide solutions through a sudden planar contraction. *J. Non-Newt. Fluid Mech.* 28 (1988) 267–285.
41. E. Ryssel and P.O. Brunn, Flow of a quasi-Newtonian fluid through a planar contraction. *J. Non-Newt. Fluid Mech.* 85 (1999) 11–27.
42. R. Mei, Flow due to an oscillating sphere and an expression for unsteady drag on the sphere at finite Reynolds number. *J. Fluid Mech.* 270 (1994) 133–174.